View metadata, citation and similar papers at core.ac.uk
brought to you by CORE
provided by Apollo

Fabrication of High-Resolution Strain Sensors Based on Wafer-Level Vacuum Packaged MEMS Resonators

Luca Belsito[1]*, Matteo Ferri[1], Fulvio Mancarella[1], Luca Masini[1], Jize Yan[2], Ashwin A. Seshia[2], Kenichi Soga[3], and Alberto Roncaglia[1]

[1]Institute of Microelectronics and Microsystems, CNR, Via Gobetti 101, I-40129 Bologna, Italy
[2]Nanoscience Centre, Department of Engineering, University of Cambridge, Cambridge, CB3 0FF, U.K.
[3]Department of Engineering, University of Cambridge, Cambridge, CB3 0FF, U.K.
*Corresponding Author – email: belsito@bo.imm.cnr.it

Abstract— **The paper reports on the fabrication and characterization of high-resolution strain sensors for structural materials based on Silicon On Insulator flexural resonators manufactured by polysilicon Low-Pressure Chemical Vapour Deposition vacuum packaging. The sensors present sensitivity of 164 Hz/με and strain resolution limit of 150 pε on steel for a measurement time of 315 ms, in both tensile and compressive strain regimes. The readout of the sensor is implemented with a transimpedance oscillator circuit implemented on Printed Circuit Board, in which a microcontroller-based reciprocal frequency counter is integrated. The performance of the sensors on steel are investigated for measurement bandwidths from 1.5 to 500 Hz and a comparison with conventional metal strain gauges is proposed.**

Keywords— Strain sensor, resonator, SOI, MEMS, wafer-level vacuum packaging.

I. INTRODUCTION

Strain sensors are widely employed in many fields of engineering in order to quantify the surface deformation of structural materials [1]. Such measurements are of paramount importance in order to determine the effect of mechanical load on a structure, evaluating its strength and resistance, and are widely applied in civil, mechanical and biomedical engineering [2]-[4]. The most widespread technology presently adopted for surface strain sensing on structural materials is metal strain gauge technology, which relies on the change in the electrical resistance of a thin metal film patterned on a plastic foil [5]. In these sensors, the electrical resistance changes due to the geometry variation in the metal pattern induced by the strain transmitted to the substrate by the underlying structure, on which the sensor has to be firmly attached, usually by glue. In order to produce an appropriate sensing signal, the sensors are commonly included in a Wheatstone bridge configuration with other reference resistors, so that the resistance variation induced on the strain gauge can be converted into a change of the bridge output voltage. In such conditions, the differential voltage signal V_{out} measured on the output of a balanced bridge composed by one sensor and three reference resistors can be expressed as:

$$V_{out} = \frac{V_{dd}}{4} GF\, \varepsilon \qquad (1)$$

where ε is the strain along the gauge axis, V_{dd} the supply voltage of the bridge and GF the gauge factor of the sensor, defined as the relative resistance variation per unit applied strain on the gauge.
It can be shown for metal strain gauges that the following equation relating bandwidth (Δf) and noise-equivalent strain (NES) at temperature T_a can be obtained [6]:

$$\frac{1}{NES}\sqrt{\Delta f} = \frac{GF\ V_{dd}}{8\sqrt{kT_a R}} \qquad (2)$$

From eq. (2), in which k is the Boltzmann constant, it clearly appears that the product between the inverse of the resolution limit of the strain sensor (which can be identified with the NES) and the square root of the measurement bandwidth is limited by the physical properties of the strain gauge (GF and R) and by the allowed voltage supply of the bridge (V_{dd}). This means that, using metal strain gauges, high resolution can only be reached by limiting the measurement bandwidth. On the other hand, if large measurement bandwidths are needed, resolution must be

sacrificed.

Eq. (2) also shows the correlation between power consumption and performances since, given the electromechanical properties of the strain gauge (GF and R), the only way to increase the value of the right hand member of eq. (2) is increasing V_{dd} and therefore the power consumption of the bridge. As a consequence of that, depending on the target resolution and bandwidth, the power consumption needed using conventional metal strain gauges can be rather high. Such limitation is particularly restrictive in applications involving battery operated systems with high-throughput data logging or performing long-term measurements.

In order to overcome these limitations, the use of Micro-Electro-Mechanical-System (MEMS) flexural resonators as strain sensors for structural materials has been proposed, dating back to the research work carried out for micromachined quartz resonant sensors [7-10]. More recently, researchers from the University of California at Berkeley developed DETF resonators operated in air driven by square-wave oscillators, and explored possible applications related to strain sensing on structural materials with such devices [11]-[14]. Another example of silicon DETF strain sensor operating at atmospheric pressure has been recently reported in [15], whereas other materials such as silicon carbide and aluminum nitride have been investigated for similar purposes [16], [17].

Compared to operation in air, the use of the resonator in vacuum environment promises better performances thanks to the elimination of gas damping effect [18], [19]. However, a durable vacuum packaging on strain sensors bonded on steel is not easily achievable by hybrid packaging techniques, as described by our group in previous research [20]-[22].

In this paper, a possible solution for the problem of vacuum packaging is proposed, based on the fabrication of Silicon On Insulator (SOI) flexural resonators with wafer-level vacuum packaging obtained by Low-Pressure Chemical Vapour Deposition (LPCVD) sealing [23].

The paper is organized as follows. In Section II, the fabrication process is described. Section III reports on the readout electronics of the resonators implemented on a Printed Circuit Board (PCB). Test results on the sensor prototypes are described in Section IV and discussed in Section V. Some conclusions are finally presented in section VI.

II. Design and Fabrication

The strain sensors were fabricated starting from four-inch SOI substrates with 25 µm thick device layer, 2 µm thick buried oxide and 500 µm thick handle layer. Both the device and handle layers were heavily doped n-type using phosphorus for the device layer (resistivity in the range 0.001-0.005 ohm cm) and antimony for the handle layer (resistivity in the range 0.005-0.008 ohm cm). The process flow described in the following section was adopted to manufacture the sensors.

A. *Fabrication process flow*

First, a 1.5 µm thick SiO_2 layer is deposited by Low-Pressure Chemical Vapour Deposition (LPCVD). Next, the geometry of the resonator is patterned on SiO_2 by Reactive Ion Etching (RIE) during process steps 2 and 3 in Fig. 1. On the pattern, a gap narrowing procedure is executed in order to increase the transduction efficiency and lower the motional resistance (step 4), before micromachining of the SOI device layer by Deep Reactive Ion Etching (DRIE) at process step 5. The gap narrowing effect is obtained by creating a spacer on the sidewalls of the SiO_2 features created at step 3 by polysilicon deposition followed by thermal oxidation and RIE etchback, as described in [24]. The micromachined geometries are then planarized by an 8 µm thick deposition of silicon oxide by LPCVD (step 6). On the planarization layer, 11 µm wide trenches are subsequently etched by Inductively Coupled Plasma (ICP) for SiO_2 up to the SOI device layer (step 7). These trenches created all around the pads of the DETF devices on the thick SiO_2 layer are then completely filled by the polysilicon/Si_3N_4/polysilicon triple stack LPCVD deposition performed at step 8, creating a lateral stop barrier for SiO_2 etching that is exploited as a guard ring around the pad areas of the resonators. In this way, the risk of loosing vacuum integrity through the pad apertures for excessive sacrificial SiO_2 etching during the release of the resonators performed at process step 12 is avoided. The thicknesses adopted for the encapsulation layers are 2.5 µm for level 1 polysilicon, 300 nm for Si_3N_4, and 4.5 µm for level 2 polysilicon. In the stack, silicon nitride is introduced in order to compensate compressive strain in LPCVD polysilicon and avoid buckling of the encapsulation, which could be dangerous for its mechanical integrity.

After deposition, small circular holes are drilled in the stack by DRIE (step 9) in order to allow the release of the resonators by SiO_2 hydrofluoric acid vapor etching at process step 12. Before HF etching, another gap narrowing

procedure is performed on the drilled holes (step 10), aimed at limiting the amount of undesired polysilicon deposited inside the vacuum package during LPCVD sealing by the 3 μm thick polysilicon deposition executed at step 13. Moreover, the pads of the resonators are also etched through all the passivation and encapsulation layers by Si DRIE and SiO_2 ICP before release (process step 11). After sealing the resonator encapsulation by polysilicon deposition (step 13), isotropic plasma Si etching is utilized to selectively remove undoped polysilicon from the pad areas (step 14). A 500 nm thick Al/Si film (with 2% of silicon) is finally deposited and patterned on the pads in order to provide electrical contacts on the resonators and allow easy wire bonding of the prototypes.

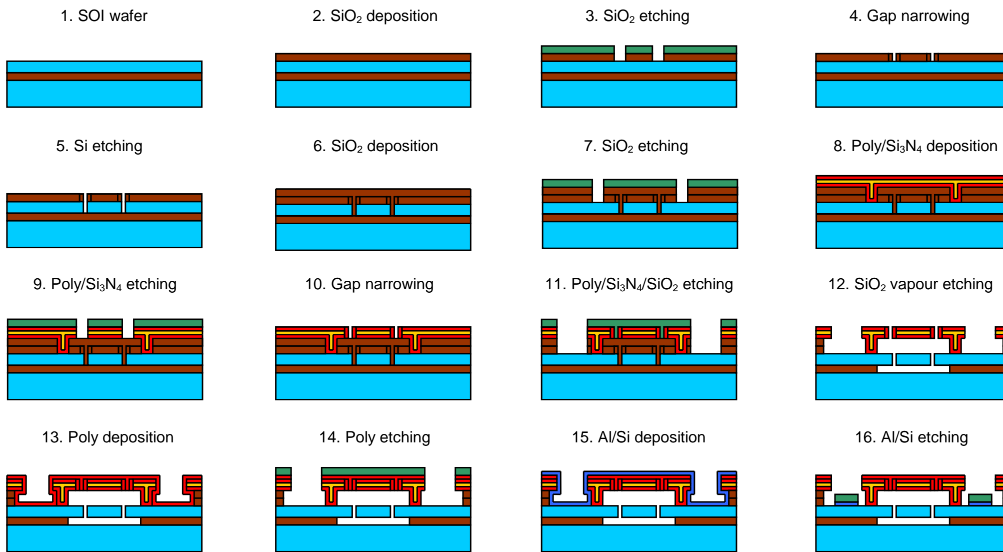

Fig. 1. Process flow for the fabrication of strain sensors based on wafer-level vacuum packaged flexural resonators.

In the described process, SiO_2 RIE at step 3 is executed by capacitively coupled plasma based on CHF_3 at a pressure of 38.5 mTorr with a gas flow of 25 sccm; Deep Reactive Ion Etching of silicon, utilized at process step 7 for micromachining of the SOI device layer and at process steps 9 and 11 for etching the polysilicon/Si_3N_4 triple stack, is carried out using a Bosch recipe based on SF_6 and C_4F_8, providing a Si etch rate around 5 μm/min, at a pressure of 30 mTorr with a gas flow of 300 and 150 sccm for SF_6 and C_4F_8 respectively; SiO_2 ICP etching at steps 7 and 11 is executed using a C_4F_8 recipe at a pressure of 4 mTorr with a gas flow of 17 sccm; HF etching utilized at step 12 for the release of the resonators is performed by placing the wafer over a cold 49% wt concentrated aqueous HF solution applying controlled heating to maintain the substrate at 40 °C for about 16 hours; Al/Si etching at step 16 is carried out by commercial aluminum etching solution from Fujifilm, a 16:1:1:2 H_3PO_4:CH_3COOH:HNO_3:H_2O mixture, heated at 35 °C. SiO_2 depositions by LPCVD at steps 2 and 6 are performed from SiH_4 and O_2 at 180 mTorr and 420 °C, with gas flows of 82 and 120 sccm for SiH_4 and O_2 respectively; undoped polysilicon at steps 8 and 13 is deposited from SiH_4 at 160 mTorr and 595 °C, with a gas flow of 80 sccm; Si_3N_4 at step 8 is obtained from SiH_2Cl_2 and NH_3 at 160 mTorr and 780 °C, with gas flows of 27 and 120 sccm for SiH_2Cl_2 and NH_3 respectively. Lithography at steps 3, 7, 9, 11 is executed by Fujifilm OiR908-35 4 μm thick fotoresist, whereas, at steps 14 and 16, Fujifilm AZ9260 10 μm thick photoresist is utilized.

B. Layout design

The typical design adopted for the strain sensors was the Double-Ended Tuning Fork (DETF) geometry shown in

Fig. 2. The operating principle of the device relies on the fact that the mechanical resonance frequency of the DETF changes upon application of axial strain; consequently, a strain sensor can be realized by integrating the resonator in a closed loop configuration as a strain-dependent oscillator. The main geometrical parameters of the resonator layout indicated in the figure are the overall length of the tuning fork (L_t), the width of the resonator tines (W_t), the width and length of the anchors (W_a and L_a, respectively), the diameter of the release holes (D_h), their spacing (L_h), the length of the parallel-plate actuation electrodes (L_e) and their air gap (W_g). The values adopted for these parameters in the design of the strain sensors are reported in Tab. 1.

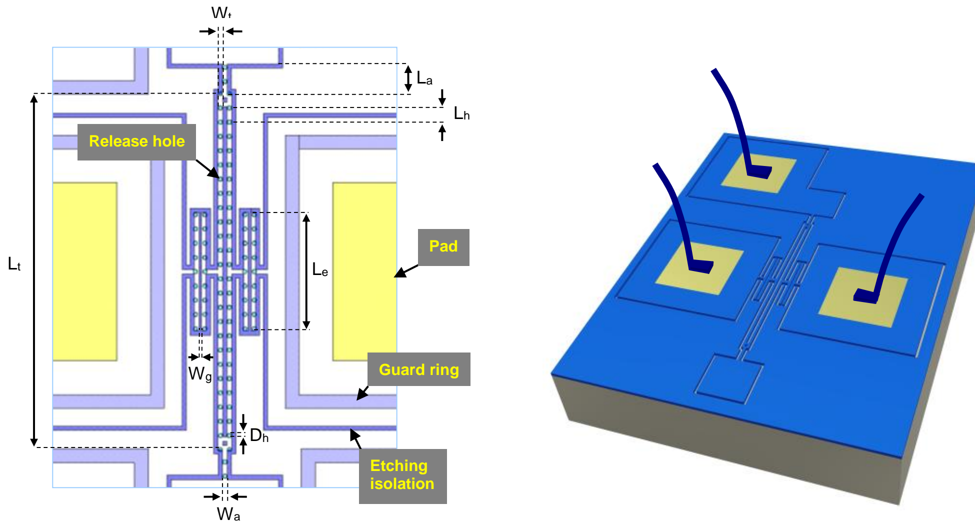

Fig. 2. Layout design (left) and 3-d representation (right) of the flexural DETF resonator.

TABLE I
GEOMETRICAL PARAMETERS ADOPTED IN THE DESIGN OF THE RESONATORS

Parameter	Values
L_t	220, 260, 300, 340, 380 µm
W_t	4, 4.5, 5, 5.5 µm
W_a	5 µm
L_a	20 µm
D_h	3.5, 3.75 µm
L_h	8, 9, 10, 11, 12 µm
L_e	100 µm
W_g	1.5, 2 µm

The Scanning Electron Microscope (SEM) image of the cross section of a fabricated sensor prototype, obtained by dicing, is reported in Fig. 3 by way of example.

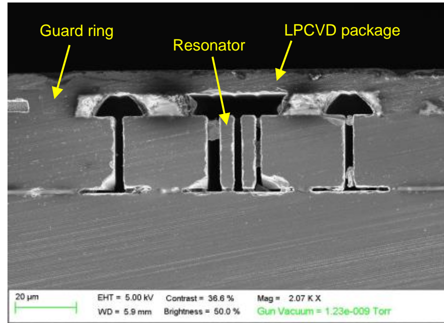

Fig. 3. Cross-section of a DETF flexural resonator fabricated with wafer-level vacuum packaging.

III. READOUT ELECTRONICS

The DETF resonator was driven by a closed loop oscillator circuit in order to operate in self oscillation mode at the desired resonance condition and the strain-dependent oscillation frequency of the circuit was measured by a digital frequency counter. The full readout electronics required by the sensor was implemented on a Printed Circuit Board (PCB) designed to operate up to three resonators in parallel (Fig. 4).

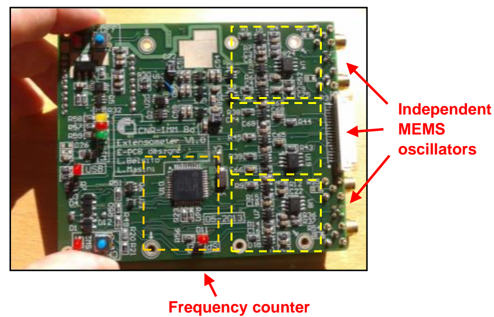

Fig. 4. PCB for operation of three resonators in parallel with integrated digital frequency counter.

A. Analog readout

The analog circuit designed to drive the MEMS resonators in closed loop is schematically represented in Fig. 5. A more detailed scheme is shown in the Appendix for the interested reader.

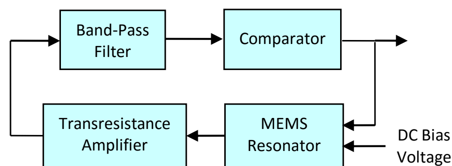

Fig. 5: Feedback scheme used for closed-loop operation of the MEMS resonant sensors.

In the circuit, the AC current generated on the mobile electrode of the resonator is first amplified by an OPA320 wideband transimpedance amplifier with low bias current from Texas Instruments (TI) and then filtered in order to reduce noise using a second-order band pass filter centered on the resonance frequency of the device (implemented with an OPA890 amplifier from TI). The central frequency of the filter is selected using a digital potentiometer controlled through Serial Peripheral Interface (SPI) communication by the system microcontroller (PIC32MX250 from Microchip), which can be used to adapt the readout electronics to MEMS resonators with different resonance frequencies. Another stage (OPA890 amplifier from TI in comparator configuration) is finally employed on the band pass filter output to limit the driving voltage on the resonator, which is applied to the fixed electrodes by using a voltage divider. In this way, possible nonlinearities coming from excessive AC voltage amplitudes on the resonator are avoided. Within the voltage divider, a manual potentiometer is utilized to select the minimum AC voltage able to sustain oscillation, in order to avoid nonlinear effects coming from excessive actuation amplitudes. Before it is applied to the MEMS, the AC signal produced by the feedback loop is added to a DC bias voltage through a bias tee constituted by a capacitance and a resistance. In order to operate properly, the designed analog front-end needs to be applied to resonators with sufficient resonance peak height, able to produce a significant motional current on the electrodes during the start-up of the oscillation in the circuit. The quality (Q) factor of the employed resonators also affects the oscillator performance because high Q values improve noise rejection in the feedback loop, reducing the phase noise of the oscillator. The power consumption of the analog readout was around 12 mW per channel.

B. Digital readout

The digital frequency counter based on reciprocal frequency measurement reported in Fig. 6 [25] was implemented on the readout PCB in order to determine the oscillation frequency of the resonators operating in closed loop.

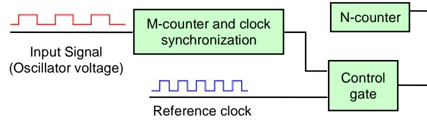

Fig. 6: Reciprocal frequency counter block diagram.

The measurement technique employs two digital counters. The first counter counts the edges of the MEMS oscillator voltage (M), the second one those of a high frequency reference clock (N) within a given acquisition time. A control circuit is employed to start the reference clock counter on the first rising edge of the input signal and stop it at the M_{th} one, according to the selected acquisition time.

After counting M wavefronts on the input signal over the acquisition time T_{aq}, the average oscillation frequency f should be ideally calculated as:

$$f = \frac{M}{T_{aq}} \qquad (3)$$

Now, the idea behind the reciprocal frequency counter measurement is using the M-counter to exactly determine the wavefront number M and the N-counter to approximately estimate the acquisition time as

$$T_{aq} \cong NT_c \qquad (4)$$

with T_c reference clock period. Since the N-counter is stopped by the control gate on the Mth rising edge of the input signal, the acquisition time estimation expressed by eq. (4) will be affected by an error whose maximum value will coincide with the clock period T_c.

By indicating such estimation error with ΔT_{aq}, we may calculate the consequent error on the calculation of f from eq. (3) as:

$$f = \frac{M}{T_{aq}^{0} + \Delta T_{aq}} \cong \frac{M}{T_{aq}^{0}}\left(1 - \frac{\Delta T_{aq}}{T_{aq}^{0}}\right) \qquad (5)$$

where T_{aq}^{0} is the exact value of the acquisition time and $\Delta T_{aq}/T_{aq}^{0}$ the relative error on frequency.
Combining eqs. (3)-(5) and considering $\Delta T_{aq} = T_c$ as a worst-case estimation of the error on acquisition time, we may write:

$$f \cong \frac{M}{NT_c} \qquad (6)$$

and

$$\Delta f \cong \frac{1}{N} f \qquad (7)$$

with Δf absolute error on frequency.
As can be inferred from eq. (7), the resolution of the frequency measurement depends on the number of clock periods counted during the acquisition time (N). Since, practically, the oscillation frequency f of the circuit is determined by the resonator, the measurement accuracy can only be enhanced by increasing N through the use of a longer acquisition time and/or a higher reference clock frequency.
As a consequence of these considerations, frequency resolution and measurement bandwidth will be correlated since fast acquisition will lead to lower resolution, whereas longer acquisition times will result in more accurate measurements.
In order to verify the validity of these theoretical considerations, the accuracy of the reciprocal frequency counter prototype was experimentally determined by measurements performed on a MEMS resonator with resonance frequency around 308 kHz. The resonator was operated with one of the closed-loop oscillator circuits on the PCB (see Fig. 4) in which the output voltage of the comparator stage was connected in parallel to two independent frequency counters (one of the same PCB and one on a different PCB). The frequency counters were implemented following the general scheme of Fig. 6 by exploiting the input capture modules of the PIC32MX250 microcontroller included in the readout board, communicating with a PC by USB interface for data acquisition. The digital readout implemented in this way presented a power consumption of roughly 65 mW when using a reference clock at 40 MHz.

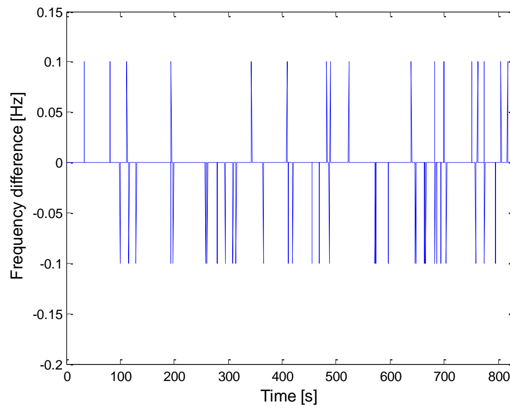

Fig. 7. Fluctuation observed on the differential frequency measured by two independent digital readout circuits.

In this experiment, the reference clock coming from the microcontroller was set to 40 MHz and the frequencies, calculated according to eq. (6), were acquired independently and simultaneously by the two identical frequency meters. Afterwards, the difference between frequency values acquired in simultaneous measurements was calculated and plotted as a function of measurement time.

On this plot, a quantized frequency fluctuation was observed, as shown in Fig. 7. Such fluctuation is expected to be completely independent of analog effects deriving from the oscillator phase noise or drift phenomena, which are cancelled on the differential signal since the same oscillator was used for the two acquisition channels and the measurements were performed simultaneously. This is also confirmed by the observed quantization of the noise, which is expected to be determined by the accuracy limitation of the frequency counter, as described by eq. (7).

In Fig. 8, the maximum fluctuation observed on the differential frequency over time intervals of 800 s with acquisition times ranging from 1 to 315 ms is reported and compared with the theoretical estimation obtained with eq. (7).

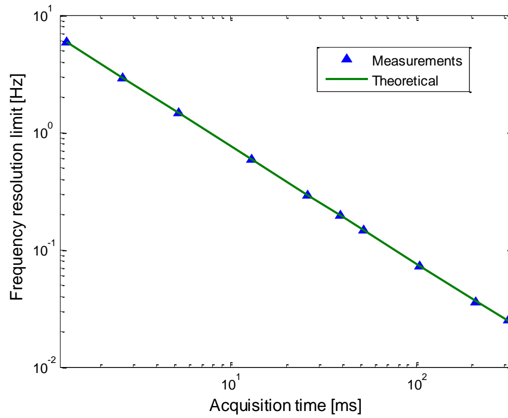

Fig. 8. Frequency resolution limit vs. acquisition time T_{aq}.

As can be seen from the plot, a good match between experimental and calculated data is obtained. Quite evidently, the frequency resolution limit steadily decreases by increasing acquisition time, in accordance with eq. (7), and a relative accuracy of 1 ppm on frequency measurement (corresponding to roughly 0.3 Hz) is obtained with an acquisition time around 25 ms.

IV. TESTING

The mechanical behavior of the resonator can be described by the motion equation of a mass-spring system, characterized by the resonator equivalent mass, its spring constant and a damping coefficient accounting for mechanisms of energy loss during oscillation [26]. From such equation, electrostatic flexural resonators operating close to their mechanical resonance frequency can be modeled as an equivalent electrical circuit constituted by a R_m, L_m, C_m series (called motional parameters) and a parallel feedthrough capacitor C_0, describing the intrinsic capacitance of the resonator electrodes and the overall parasitic effects (Fig. 9).

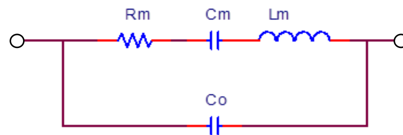

Figure 9. Equivalent electrical model of the DETF resonator operated in one port configuration.

The motional parameters of the resonator can be expressed as [27]:

$$L_m = \frac{m_{eq}}{\eta^2} \quad (8), \qquad R_m = \frac{m_{eq}\omega_0}{Q\eta^2} \quad (9), \qquad C_m = \frac{\eta^2}{\omega_0^2 m_{eq}} \quad (10)$$

where m_{eq} is the equivalent mass of the resonator, ω_0 its resonance frequency, Q the mechanical quality factor (defined as the ratio of the amount of energy stored and the one lost in one vibration cycle of the resonator), and η the electromechanical coupling factor given by:

$$\eta = V_{DC} \frac{\varepsilon A}{d^2} \qquad (11)$$

where V_{DC} is the DC bias voltage applied between the mobile and fixed electrodes of the resonator, A the electrode area and d the electrostatic coupling gap.

In order to properly operate the resonator in closed loop, the AC current flowing on the R_m, L_m, C_m series in the circuit of Fig. 9 should be maximized with respect to the one on the parallel feedthrough capacitance C_0. Since, for $\omega = \omega_0$, the impedance of the R_m, L_m, C_m series is purely resistive, R_m should be minimized to this purpose. A very effective way to minimize R_m is designing resonators with small coupling gap d since, as can be derived by combining eqs. (9) and (11), R_m is proportional to d^4. When the motional impedance is low with respect to the one associated to the parallel feedthrough capacitance C_0, a high resonance peak is observed in the open-loop characteristics of the resonator. Open-loop measurements were exploited to determine the equivalent electrical parameters expressed by eqs. (8)-(11) on the fabricated prototypes.

A. Open-loop testing

The manufactured devices were tested by wafer-level open loop measurements using a setup composed by a network analyzer (Anritsu MS2036C) and a transimpedance amplifier based on OPA656 from TI (Fig. 10).

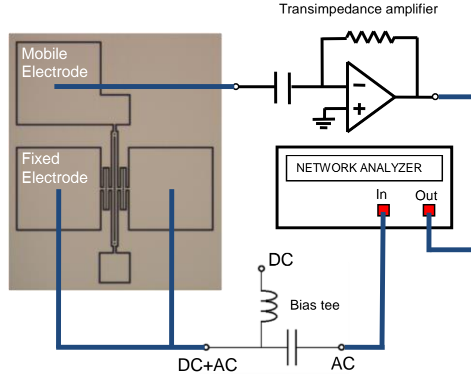

Fig. 10. Open loop resonator test setup.

In the measurements, the two fixed electrodes of the resonators were electrically shorted together and connected to a small-signal AC voltage, added to a proper DC bias through an external bias tee, and the resulting AC current on the mobile electrode was measured after being converted into a voltage by the transimpedance amplifier. In such one-port setup, the beams of the resonators were forced to oscillate in opposite direction (corresponding to the out of phase resonance mode shown in Fig. 11, calculated from finite-element simulations by COMSOL® [28]).

A consistent number of devices (about 400) on a processed wafer were tested in open-loop with the described setup in order to investigate the yield of the fabrication process, which was found to be above 90%. The measurements were realized at wafer level by means of an automatic probing system using RF tips to reduce off-chip

parasitic capacitances. In particular, resonators with beam widths in the range 4÷5.5 µm, beam lengths from 220 to 380 µm and nominal coupling gap before narrowing of 1.5 and 2 µm were measured to calculate the yield of the process.

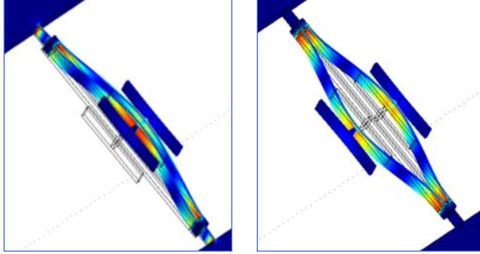

Fig. 11. In phase (left) and out of phase (right) resonator modes.

The same measurements were also utilized to determine the electromechanical characteristics of the resonators. Low feedthrough capacitance and resonance peaks up to 25 dB above the feedthrough baseline were measured for a DC bias voltage of 5 V. In particular, the resonators with tine width W_t of 4 um coupling gaps W_g of 1.5 µm showed the best performances in terms of motional resistance and Q factor. Moreover, the length of the beams turned out to impact the resonators' performances with particular concern to nonlinear effects, since the longer beams showed pronounced nonlinearities even at low AC driving voltages. For this reason, resonators designed with a tine length L_t of 300 µm, tine width W_t of 4 µm, and nominal coupling gap W_g of 1.5 µm were chosen to be employed in the closed loop configuration, in order to enable the use of sufficiently high AC driving voltages and consequently increase the motional current on the devices, avoiding nonlinear effects. The open-loop admittance amplitude spectra measured on a resonator prototype corresponding to this geometry and obtained using different DC bias voltages are shown in Fig. 12. The corresponding electromechanical parameters, extrapolated by the experimental data for a V_{DC} = 3 V, are reported in Table II.

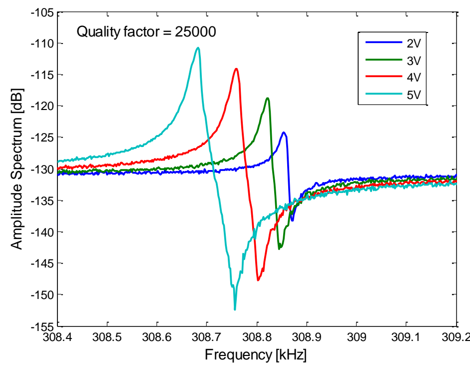

Fig. 12. Amplitude admittance spectra of a DETF resonator with L_t = 300 µm, W_t = 4 µm, W_g = 1.5 µm for different V_{DC} voltages.

In order to determine such parameters from the open-loop measurements, the following formulae were utilized [29]:

$$R_m = \frac{1}{4\pi Q\left(f_p - f_s\right)C_0} \quad (12)$$

$$C_m = \frac{f_p - f_s}{f_s} \quad (13)$$

$$L_m = \frac{1}{4\pi^2 f_s^2 C_m} \quad (14)$$

where f_s and f_p are the series and parallel resonance frequencies, respectively corresponding to the maxima and minima of the open-loop spectra reported in Fig. 12.

In the extrapolation procedure, the feedthrough capacitance C_0 is first determined by setting the DC bias of the resonator to zero and fitting the open-loop measurement acquired in this condition by modeling the device with C_0 only. Once determined C_0 by the best-fit of the measured spectrum for $V_{DC} = 0$, the contribution of the feedthrough capacitor is subtracted from the admittance spectra measured for nonzero values of the DC bias, in order to derive the net contribution of the R_m, L_m, C_m series to the resonator admittance. From this processed spectrum, the resonator quality factor is calculated from the Full Width Half Maximum (FWHM) of the resonant peak. Starting from the values of C_0 and Q determined in this way, all the other parameters expressed by eqs. (12)-(14) can be calculated from the series and parallel resonance frequencies f_s and f_p derived from the raw spectra (Tab. II).

TABLE II
EQUIVALENT ELECTROMECHANICAL PARAMETERS OF DETF RESONATOR WITH $L_T = 300$ μM, $W_T = 4$ μM, $W_G = 1.5$ μM, $V_{DC} = 3$ V

Parameter	Symbol	Value
Motional resistance	R_m	960 kΩ
Motional inductance	L_m	1.13 kH
Motional capacitance	C_m	0.023 fF
Feedthrough capacitance	C_0	0.15 pF

The quality factors obtained from the measurements in this way were in the range 10,000-30,000, depending on the resonator geometry. In determining the quality factors, measurements with DC bias levels around 3 V were utilized in order to maintain the resonator in linear regime of operation. By comparison with similar measurements performed on unpackaged resonators within a macroscopic vacuum chamber, the vacuum level within the LPCVD encapsulation was estimated to be around 120 mTorr. In such vacuum conditions, the squeeze film air damping between the actuation electrodes of the resonator is expected to be unimportant, whereas the thermoelastic damping due to the deformation of the mechanical structure during vibration will be dominant. This was confirmed by the dependence of the Q factors measured on the geometry of the differently designed resonators, particularly on tine width. Since the device layer of the SOI substrate is essentially free of residual stress, the resonant frequencies and Q factor values on the devices showed a very small dispersion on the wafer area, with a repeatability level around few percent on identical devices on different positions on the wafer. The residual stress of the polysilicon/Si_3N_4 encapsulation, in this respect, is not expected to have a direct impact on the performance of the device since it is anchored to the bulk substrate and consequently mechanically decoupled from the resonator.

Commented [a1]: The reviewers may ask to see this data to confirm the impact of thermo-elastic damping and to ensure that the Q's are indeed independent of pressure.

B. Load tests in closed loop

When the DETF resonator is subjected to strain, its mechanical resonance frequency changes. For small deformations, such resonance frequency variation Δf can be expressed as [30]:

$$\frac{\Delta f}{f} = 0.075 \frac{l^2}{w^2} \varepsilon \quad (15)$$

where l, w are respectively the length and width of the DETF tines and ε is the axial strain.

In order to estimate the strain sensitivity of the resonators, a four-point bending test setup was utilized (Fig. 13), consisting of a 2 mm thick steel bar onto which the resonator chip was bonded by epoxy glue (Torr Seal from Varian).

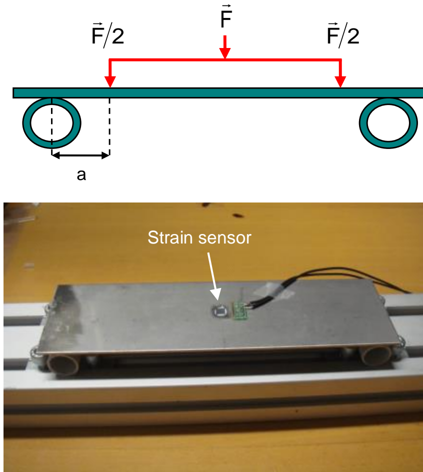

Fig. 13. Bending test setup utilized to characterize the strain sensors.

As shown in Fig. 13, a controlled force was applied on the bar according to the four-point bending test standard, using calibrated weights on a thin U-shaped steel support, able to apply a load within two 1 mm wide areas transversally distributed on the whole bar width, which can be approximated as a force applied on two linear pins placed on the bar in transverse direction. During the load tests, the bar was sustained by two cylindrical supports on which the bar was left free to slide and rotate.

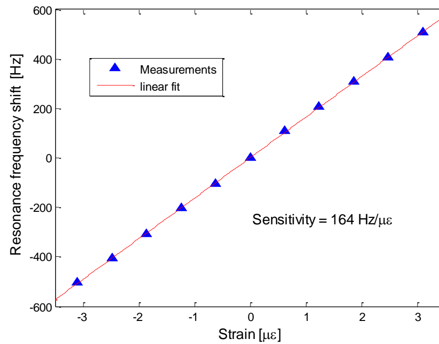

Fig. 14. Calibration curve obtained in the bending tests on the resonant strain sensor.

From theoretical considerations, the axial strain ε generated on the inner part of the bar with respect to the linear loading pins in such bending setup is expected to be constant and approximately described by the following formula [31]:

$$\varepsilon = \frac{3Fa}{Ebd^2} \qquad (16)$$

where F is the total force applied to the steel beam on the loading areas, modeled as linear pins, a the distance between the loading and supporting pins (5 cm), d and b the thickness (2 mm) and width (7 cm) of the bar respectively, and E steel Young's Modulus.

The validity of eq. (16) was verified by measuring the strain generated on the bar by loading the bending setup using a commercial metal strain gauge from Vishay attached to the bar by cyanoacrylate glue. The experimental results were found to be in good agreement with the theoretical prediction of eq. (16) assuming E = 196 GPa.

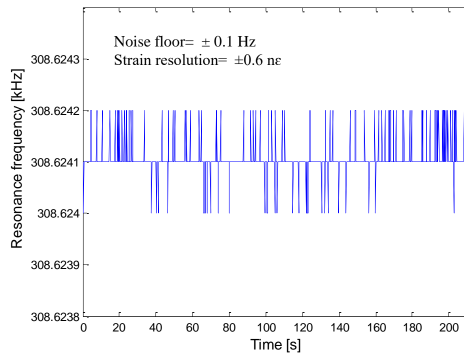

Fig. 15. Closed loop resonance frequency measured on the strain sensor with an acquisition time of 75 ms.

The bending tests on the resonant strain sensor were performed by applying increasing loads on the bending setup and measuring the induced frequency shift on the bonded resonator operating in closed loop compared to the unstrained condition. A typical result obtained in these tests on the resonator geometry of choice is reported in Fig. 14, using eq. (16) to calculate the applied strain, in which negative values are utilized for compressive strain. From the slope of the curve, a sensitivity around 164 Hz/με can be estimated.

Such sensitivity is referred to the strain generated on the bar, while the one on the sensor is expected to be lower due to strain transmission limitations of the steel support/glue/silicon chip system. From finite-element simulations performed with COMSOL® [28], the expected sensitivity of the plain resonant sensor turned out to be around 180 Hz/με. This value is reasonably in line with the experimental results, even though the effect of the structure bending and the strain transmission from the bar to the sensor should be also taken into account. From other simulations performed on the steel/glue/silicon system, the strain transmission ratio was actually observed to increase by decreasing the thickness of the silicon chip, while the thickness of the glue layer was less influential.

Compared to previous results obtained using DETF devices with hybrid vacuum packaging [22], the sensitivity obtained here is remarkably higher. This result is partly due to design optimization of the resonators but also to the fact that the chip-level packaging does not introduce any significant stiffening on the sensor or on the structure under measurement. This was not the case with the previously proposed hybrid packaging technique which was based on rather bulk steel capping structures sealed by vacuum glue [20]. Other advantages coming with the use of the thin-film encapsulation are the enhanced durability of vacuum and the allowed miniaturization of the devices in on-field applications.

In order to derive the resolution of the strain sensor, the frequency noise of the MEMS oscillator/frequency counter system needs to be estimated. In Fig. 15, the frequency noise observed using an acquisition time of 75 ms on the frequency meter output and a 40 MHz reference clock is shown by way of example. As can be observed, noise is dominated by the digital error of the frequency counter, which overwhelms the phase noise of the MEMS oscillator.

The strain resolution limit of the resonant sensor was estimated by calculating the maximum frequency jitter observed over an interval of 10 sec and reporting this value to an equivalent strain using the sensitivity calibration

curve of Fig. 14. This operation was repeated for different values of the frequency meter acquisition time ranging from 1 to 315 ms. The results of such measurements are reported in Fig. 16.

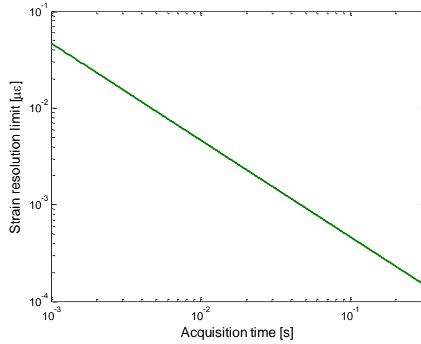

Fig. 16. Strain sensor resolution limit vs. frequency meter acquisition time.

As can be observed, the curve is similar to the one obtained in the differential frequency noise test previously discussed and reported in Fig. 8. This confirms that the digital noise introduced by the frequency meter is dominant over the oscillator phase noise on the whole range of acquisition times investigated. Consequently, a linear decrease of the strain resolution limit is obtained increasing the acquisition time of the frequency meter, and a resolution around 150 pε is obtained with the maximum acquisition time investigated of 315 ms.

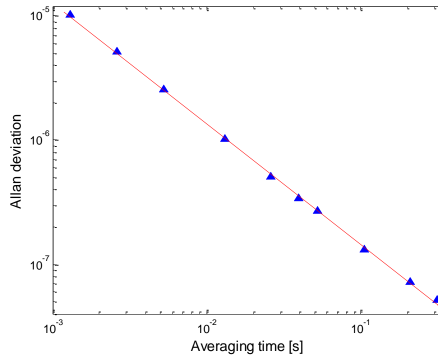

Fig. 17. Strain sensor Allan deviation vs. averaging time.

Such result was also supported by the calculation of the Allan deviation on the MEMS oscillator-frequency counter system, reported in Fig. 17 versus averaging time. As can be observed from the plot, the system shows Allan deviation values below 10^{-7} with averaging times larger than 200 ms and the curve is linear due to the prevalence of the frequency jitter coming from the quantization error of the digital counter. This confirms that phase noise effects are not significant even in the higher T_{aq} points reported in the strain resolution curve of Fig. 17, derived from straightforward observation of the frequency jitter on the sensor signal.

Further tests were carried out in order to investigate the high-strain behavior of the sensors, which is expected to be affected by the shear strength limit of the epoxy glue utilized to bond the sensor to the steel specimen. In such tests, Torr Seal glue was utilized as well, applying increasing loads on the bending test setup of Fig. 13 up to the appearance of an irreversible change on the sensor sensitivity, in order to determine the maximum detectable strain measurable with the resonant sensor.

The result of such test is reported in Fig. 18. As may be observed, the low-strain sensitivity characteristic shown

in Fig. 14 is maintained up to strain levels around 115 με. After applying the maximum strain level of 250 με, a visible loss of sensitivity is observed in the plot. Subsequent measurements confirmed that the observed effect was irreversible, most probably owing to a failure of the epoxy glue for excessive shear stress application on the bonding interface.

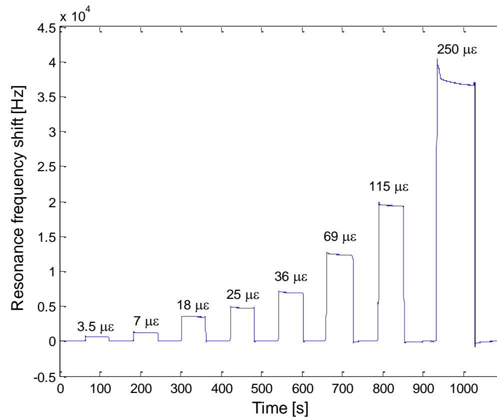

Fig. 18. High-strain bending test results.

V. DISCUSSION

In order to compare the results obtained with the resonant sensor to conventional metal strain gauges, the NES of a 120 Ω resistive gauge with GF = 2.1 and in a balanced Wheatstone bridge with V_{dd} = 3 V connected to a low noise instrumentation amplifier (AN163 from TI with gain set to 10) was calculated by Pspice simulation, taking into account Johnson and Flicker noise coming from the resistors and the amplifier.

The simulated noise spectral density was then integrated on a range compatible with increasing measurement acquisition times, in order to obtain a strain resolution limit/measurement time plot similar the one measured on the resonant strain sensor. The result obtained is reported in Fig. 19, in which the simulated curve for the conventional strain gauge and the measurements on the resonant strain sensor prototype are compared.

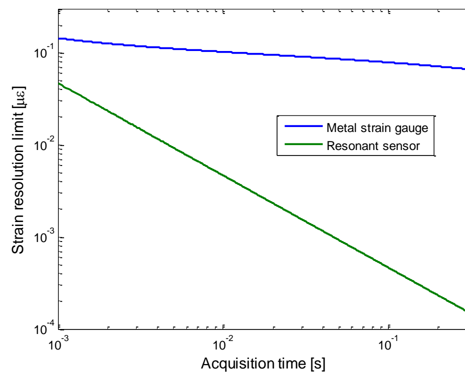

Fig. 19. Comparison of the strain resolution obtained with conventional strain gauge (simulated data) and resonant strain sensor (measurements).

As can be observed, a better trade-off between resolution and measurement bandwidth is obtained using the resonant strain sensor, with an improvement factor larger than one order of magnitude on resolution limit for acquisition times above 5 ms. It is worth noticing that the result shown is obtained starting from a best-case calculation of the noise on the conventional strain gauge since the effect of electromagnetic interferences and power supply noise were not taken into account in the model. Such effects are well known to decrease the noise performance of resistive sensors in real world applications, compared to the sole effect of Flicker and Johnson noise considered in the calculation.

Another important consideration concerns the fact that, as reported previously, the resolution of the resonant strain sensor in the range of measurement times of interest for most practical strain measurements is limited by the performance of the frequency meter. This means that the resolution of the sensor could be improved by simply adopting a more advanced circuit solution for digital frequency measurement, such as low-frequency modulation techniques of the oscillator signal in order to reduce the error expressed by eq. (7) [32].

Concerning power consumption, since no DC current needs to be employed in the resonator, it is almost completely due to the electronic readout. In the present prototype, PCB implementation of the analog circuit for closed-loop operation of the resonator is responsible for the remarkable power consumption of 12 mW per sensor. Possible integration of such analog readout on Application-Specific Integrated Circuit (ASIC), as already presented for MEMS reference clocks [33], is expected to provide large benefits in terms of power consumption. Referring to the digital part of the readout, which is responsible for the highest power consumption due to the presence of the microcontroller (65 mW), some power saving could be obtained by implementing the reciprocal digital frequency counter by FPGA technology using a properly designed circuit employing a minimum number of digital components in place of the microcontroller. Even larger improvements could be achieved by integrating the digital readout on the same ASIC using a mixed signal CMOS technology.

VI. CONCLUSIONS

Resonant strain sensors manufactured by SOI MEMS technology with wafer level vacuum encapsulation have been presented. The devices, constituted by parallel-plate DETF flexural resonators, were characterized in open loop in order to determine the process yield, which was found to be above 90 %. Thanks to the resonator design, with particular concern to the scaling of the electrostatic coupling gap of the electrodes, low values of the motional resistance on the devices were obtained for DC bias voltages below 5 V and mechanical Q factors up to 30,000 have been measured.

Resonators with a tine length of 300 μm, tine width of 4 μm and nominal coupling gap of 1.5 μm were selected for the closed-loop tests performed using a PCB readout electronics implementing a transimpedance MEMS oscillator integrated with a microcontroller-based reciprocal frequency meter, yielding strain sensitivity on steel of 164 Hz/με and a strain resolution limit of 150 pε, obtained for a measurement time of 315 ms. Bending tests in the high-strain regime up to 115 με were successfully performed with the MEMS sensors bonded on steel by epoxy Torr Seal glue showing the same sensitivity measured for low strain levels, whereas a failure of the adhesive bonding and a consequent irreversible decrease in sensitivity was observed by applying a strain level around 250 με, probably owing to excessive shear stress on the glue. Possible improvements of the sensor dynamic range may be expected by using higher shear strength glues for the silicon/steel bonding.

The strain resolution limit of the resonant sensors utilized with the described readout was found to be completely determined by the digital noise introduced by the frequency meter, showing a linear dependence on the inverse of the acquisition time utilized in the measurements. For this reason, further improvements on the strain resolution of these sensors are expected from the possible adoption of more advanced frequency metering techniques in the readout.

APPENDIX

The detailed scheme of the analog circuit utilized for the closed-loop operation of the resonant strain sensor is reported in Fig. 20 for the interested reader.

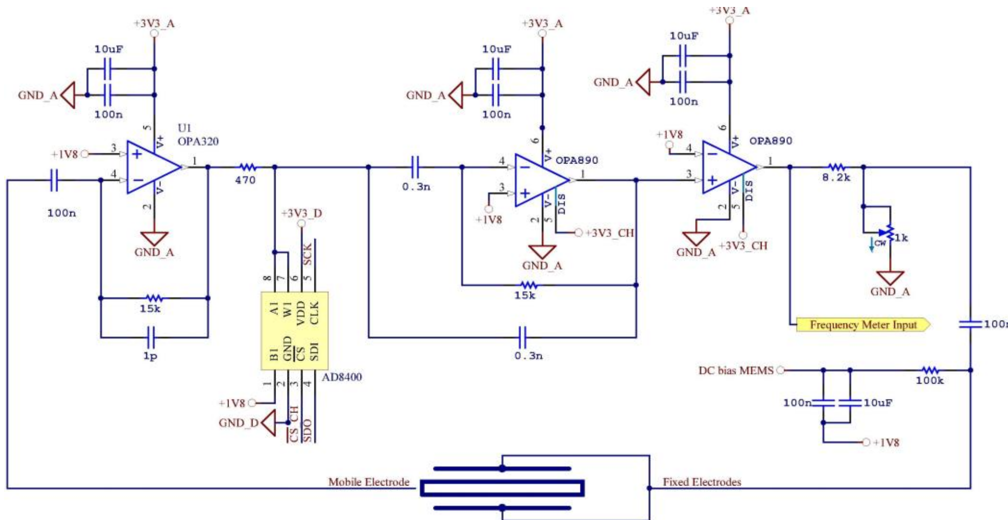

Figure 20: Detailed circuit scheme of the analog circuit used to operate the MEMS resonator in closed loop.

ACKNOWLEDGMENT

The contribution of Mr. Filippo Bonafè, Mr. Fabrizio Tamarri, Mr. Michele Sanmartin and Mr. Giulio Pizzochero in the clean room processing employed for the manufacturing of the MEMS sensors is acknowledged. The contribution of Dr. Michele Bellettato in sample preparation is also acknowledged.

REFERENCES

[1] L. Belsito, M. Ferri, F. Mancarella, A. Roncaglia, J. Yan, A. A. Seshia, K. Soga, "High-resolution strain sensing on steel by silicon-on-insulator flexural resonators fabricated with chip-level vacuum packaging", in *Tech. Digest of TRANSDUCERS and EUROSENSORS 2013*, Barcelona, Spain, 2013, pp. 992-995.

[2] B. Nordgren, J. Hall, A. Andersson, "Development of methods for registration of the force exerted by hand fingers in industrial work", *Appl. Ergon.*, vol. 25, no. 6, 1994, pp. 393-394.

[3] K. P. Speer, X. G. Deng, S. Borrero, P. A. Torzilli, D. A. Altchek, R. F. Warren, "Biomechanical evaluation of a simulated Bankart lesion", *J. Bone Joint Surg. Am.*, vol. 76A, no. 12, 1994, pp. 1819-1826.

[4] R. S. Senanayake, I. M. Cole, S. Thiruvarudchelvan, "The application of computational and experimental-techniques to metal deformation in cold roll forming", *J. Mater. Process. Tech.*, vol. 45, no. 1-4, 1994, pp. 155-160.

[5] M. Brauwers, F. Brouers, "Temperature and strain effect on electrical-resistivity of transition-metal alloys - application to strain-gauges", *J. Phys. F Met. Phys.*, vol. 6, no. 7, 1976, pp. 1331-1339.

[6] J. C. Doll, S.-J. Park, B. L. Pruitta, "Design optimization of piezoresistive cantilevers for force sensing in air and water", *J. Appl. Phys.*, vol. 106, no. 6, 2009, Art. N. 064310.

[7] R. M. Langdon, "Resonator sensors-a review", *J. Phys. E Sci. Instrum.*, vol. 18, no. 2, pp. 103-115, Feb. 1985.

[8] E. P. Eernisse, R. W. Ward, R. B. Wiggins, "Survey Of Quartz Bulk Resonator Sensor Technologies", *IEEE T. Ultrason. Ferr.*, vol. 35, no. 3, 1998, pp. 323-330.

[9] L. D. Clayton, E. P. Eernisse, R. W. Ward, R. B. Wiggins, "Miniature Crystalline Quartz Electromechanical Structures", *Sensors Actuators*, vol. 20, no. 1-2, 1989, pp. 171-177.

[10] S. P. Beeby, G. Ensell, B. R. Baker, M. J. Tudor, N. M. White, "Micromachined silicon resonant strain gauges fabricated using SOI wafer technology", *J. Microelectromech. S.*, vol. 9, no. 1, 2000, pp. 104-111.

[11] K. E. Wojciechowski, B. E. Baser, A. P. Pisano, "A MEMS resonant strain sensor operated in air", in *Proceedings of MEMS2004*, Maastricht, Netherlands, 2004, pp. 841-845.

[12] M. W. Chan, D. R. Myers, B. D. Sosnowchik, L. Lin, A. P. Pisano, "Localized strain sensing using high spatial resolution, highly-sensitive MEMS resonant strain gauges for failure prevention", *Tech. Digest of TRANSDUCERS 2011*, Beijing, China, 2011, pp. 2859-2862.

[13] B. D. Sosnowchik, R. G. Azevedo, D. R. Myers, M. W. Chan, A. P. Pisano, L. Lin, "Rapid silicon-to-steel bonding by induction heating for MEMS strain sensors*", J. Microelectromech. S.*, vol. 21, no. 2, 2012, pp. 497-506.

[14] D. R. Myers, M. W. Chan, G. Vigevani, B. D. Sosnowchik, R.G. Azevedo, A.V. Jog, L. Lin, A.P. Pisano, "Torque measurements of an automotive halfshaft using micro double-ended tuning fork strain gauges", *Sensor. Actuat. A-Phys.*, vol. 204, 2013, pp. 79-87.

[15] W. Wei, F. Yu, W. You, D. Liu, H. Yang, X. Li, "Double-ended tuning fork resonant strain sensor operated in atmospheric environment using a galvanic protection technique", *Tech. Digest of TRANSDUCERS 2015*, Anchorage, USA, 2015, pp. 1207-1210.

[16] D. R. Myers, R. G. Azevedo, L. Chen, M. Mehregany, A. P. Pisano, "Passive substrate temperature compensation of doubly anchored double-ended tuning forks", (2012) *J. Microelectromech. S.*, vol. 21, no. 6, 2012, pp. 1321-1328.

[17] F.T. Goericke, A. P. Pisano, "Aluminum nitride high temperature strain sensors", Proceedings of the 9th International Workshop on Structural Health Monitoring, IWSHM 2013, Stanford, USA, 2013, pp. 2267-2274.

[18] K. Azgin, T. Akin, L. Valdevit, "Ultrahigh-dynamic-range resonant MEMS load cells for micromechanical test frames", *Journal of Microelectromechanical Systems*, vol. 21, no. 6, 2012, pp. 1519-1529.

[19] X. Zou, A. A. Seshia, "The impact of damping on the frequency stability of nonlinear MEMS oscillators", *J. Microelectromech. S.*, vol. 24, no. 3, 2015, pp. 537-544.

[20] M. Ferri, S. Cristiani, Y. Kobayashi, K. Soga, A. Roncaglia, "A packaging technique for silicon MEMS strain sensors on steel", in *Proceedings of IEEE SENSORS2008*, Lecce, Italy, 2008, pp. 1524-1527.

[21] M. Ferri, F. Mancarella, A. A. Seshia, J. Ransley, K. Soga, J. Zalesky, A. Roncaglia, "Fabrication and packaging techniques for the application of MEMS strain sensors to wireless crack monitoring in ageing civil infrastructures", *Smart Struct. Syst.*, vol. 6, no. 3, 2010, pp. 225-238.

[22] M. Ferri, F. Mancarella, L. Belsito, A. Roncaglia, J. Yan, A. A. Seshia, K. Soga, J. Zalesky, "Strain sensing on steel surfaces using vacuum packaged MEMS resonators", in *Procedia Engineering*, vol. 5, Proceedings of Eurosensors XXIV, Linz, Austria, 2010, pp. 1426–1429.

[23] B. Kim, R. N. Candler, M. A. Hopcroft, M. Agarwal, W.-T. Park, T. W. Kenny, "Frequency stability of wafer-scale film encapsulated silicon-based MEMS resonators", *Sensor. Actuat. A-Phys.*, vol. 136, no. 1, 2007, pp. 125–131.

[24] M. Ferri, F. Mancarella, A. Roncaglia, J. Ransley, J. Yan, A. Seshia, "Fabrication of DETF sensors in SOI technology with submicron air gaps using a maskless line narrowing technique", Proceedings of IEEE Sensors 2008, art. no. 4716640, 2008, pp. 1131-1134.

[25] S. Johansson, "New frequency counting principle improves resolution", in *Proceedings of FCS 2005*, Vancouver, Canada, 2005, pp. 628-635.

[26] H. A. C. Tilmans, "Equivalent circuit representation of electro-mechanical transducers: I. Lumped-parameter systems", *J. Micromech. Microeng.*, vol. 6, no. 1, 1996, pp. 157-176.

[27] J. T. M. van Beek, R. Puers, "A review of MEMS oscillators for frequency reference and timing applications", *Journal of Micromechanics and Microengineering*, vol 22, no. 1, 2012, Art. N. 013001.

[28] http://www.comsol.com

[29] J. R. Clark, W.-T. Hsu, and C. T.-C. Nguyen, "Measurement techniques for capacitively-transduced VHF-to-UHF micromechanical resonators" Digest of Technical Papers, 11th Int. Conf. on Solid-State Sensors & Actuators (Transducers'01), Munich, Germany, June 10-14, 2001, pp. 1118-1121.

[30] J.E.-Y. Lee, B. Bahreyni, A. A. Seshia, "An axial strain modulated double-ended tuning fork electrometer", *Sensor. Actuat. A-Phys.*, vol. 148, no. 2, 2008, pp. 395-400.

[31] J. M. Gere, S. P. Timoshenko, "Appendix G: Deflections and Slopes of Beams", in *Mechanics of Materials*, 4th ed., PWS Publishing Company, Boston.

[32] B. Bahreyni, C. Shafai, "Oscillator and frequency-shift measurement circuit topologies for micromachined resonant devices", *Sensor. Actuat. A-Phys.*, vol. 137, no. 1, 2007, pp. 74-80.

[33] K. Sundaresan, G. K. Ho, S. Pourkamali, F. Ayazi, "Electronically Temperature Compensated Silicon Bulk Acoustic Resonator Reference Oscillators", *IEEE J. Solid-St. Circ.*, vol. 42, no. 6, 2007 pp. 1425-1434.